Supporting Information for

Surface Defects Induced Polarization Manipulation in Cu_2SnS_3 for Boosting Electrochemical CO_2 Reduction

Haihua Wang, Ning Wen, Yupeng Li, Xiuling Jiao, Yuguo Xia, and Dairong Chen**

National Engineering Research Center for Colloidal Materials, School of Chemistry and Chemical Engineering, Shandong University, 250100, Jinan, Shandong, China

E-mail: xyg@sdu.edu.cn; cdr@sdu.edu.cn

1. Experimental Section

1.1 Characterizations

Employing Cu Kα radiation (λ = 1.5418 Å), diffraction patterns from powder X-ray diffraction (pXRD) were obtained with a Bruker AXS D8 diffractometer set up in Bragg-Brentano geometry. Field-emission scanning electron microscopy (FE-SEM, SU8010) and transmission electron microscopy (TEM, JEOL JEM-1011) were used to investigate the structural morphology and microstructure. Furthermore, precise lattice structures were revealed using spherical aberration-corrected TEM (FEI Themis Z) in conjunction with high-resolution transmission electron microscopy (HRTEM, JEOL JEM-2100).

X-ray photoelectron spectroscopy (XPS) measurements were performed employing a Thermo Scientific K-Alpha system, with an Al Kα x-ray source and a pass energy setting of 30.0 eV. Electron spin resonance (ESR) spectra were collected using a JEOL JES-X320 instrument at room temperature (300 K) with a microwave frequency of 9165.365 MHz. Surface-enhanced infrared absorption spectroscopy (SEIRAS) was conducted using a Thermo Nicolet 8700 spectrometer equipped with a liquid nitrogen-cooled mercury cadmium telluride (MCT) detector.

1.2 H-type cell system CO_2RR measurements

Electrochemical assays were performed using a CHI 660E electrochemical workstation within an airtight, dual-chamber cell. Separation of the compartments was achieved via a proton exchange membrane, and the cell was filled with a 2 M $KHCO_3$ electrolytic solution. Counter and reference electrodes were implemented using a platinum wire and an Ag/AgCl setup, respectively. The working electrode was

fabricated by dispersive application of a catalytic layer onto titanium mesh. The electrodes were prepared using N-methyl-2-pyrrolidone as the solvent, carbon black as the conductive agent and Nafion as the binder, with an 8:1 ratio of catalyst to conductive agent, and all four were mixed by grinding to form a homogeneous ink. This mixture was then layered onto a pre-conditioned titanium mesh and left to dry under vacuum at 60 °C for an overnight duration. The 2 M $KHCO_3$ electrolyte was pre-equilibrated with CO_2 for 30 minutes to establish a saturated solution at a stable equilibrium, leading to a resultant pH of approximately 7.45. For the electrochemical processes, CO_2 gas was continuously fed into the H-type cell at 20 mL-min^{-1} using a mass flow controller.

1.3 Flow cell system CO_2RR measurements

The meticulously constructed flow cell system comprises a hermetically sealed CO_2 gas chamber and two liquid compartments separated by channels measuring 2 cm × 0.5 cm × 0.3 cm. After careful evaluation, the effective working area of the gas diffusion electrodes (GDEs) was determined to be 2 cm × 0.5 cm. The system is designed to ensure separation between the CO_2 gas and the 2 M $KHCO_3$ liquid electrolyte via the GDEs, with an anion exchange membrane (German Forma 3PK-130) maintaining separation between the catholyte and anolyte. Electrochemical testing was conducted within a three-electrode arrangement, utilizing Ag/AgCl and nickel foam as the reference and counter electrodes, respectively. A consistent blend of 5 mg of the synthesized catalyst, 1 mg of carbon black, 20 μL of 5 wt% Nafion, and 20 μL of N-methyl-2-pyrrolidone was homogenized into an ink, then evenly applied to the gas

diffusion layer with the dimensions of 3 cm × 3 cm, achieving a catalyst loading density of 1 mg cm^{-2}. The GDEs were subsequently cut to 3 cm × 1 cm and dried at 60 °C under vacuum conditions. A regulated flow rate of 20 mL min^{-1} for CO_2 gas was achieved through a mass flow controller.

Assessment of gas effluents from the cathode compartment was conducted using a gas chromatograph (FuLi 9790Plus) fitted with a thermal conductivity detector (TCD) and a flame ionization detector (FID). Concurrently, liquid by-products were scrutinized using ^1H NMR spectroscopy with a Bruker Ascend 400 MHz instrument. For the collection of liquid-phase samples, 300 µL of the electrolyte was mixed with 300 µL of a DMSO-D_2O solution. Linear sweep voltammetry was performed over a potential span from 0.2 V to -1.2 V vs. RHE at a scan rate of 10 mV s^{-1}. Electrochemical impedance spectroscopy (EIS) analyses were executed at a fixed potential of 0.2 V vs. RHE, across a frequency spectrum of 1 Hz to 1000 kHz. Potentials obtained during electrochemical examinations were converted to the reversible hydrogen electrode (RHE) scale using the Nernst equation: $E_{RHE} = E_{(Ag/AgCl)} + 0.21 + 0.0591 \times pH$.

1.4 Computational Methods

Density functional theory (DFT) computations were conducted employing the projected augmented wave (PAW) methodology, as delineated within the Vienna Ab-initio Simulation Package (VASP)[1-2]. Utilization of the generalized gradient approximation (GGA) for the exchange-correction function was predicated on the Perdew-Burke-Ernzerhof (PBE) functional; the plane-wave basis for the wave functions encompassed an energy truncation of 520 eV. To appropriately represent the notable

on-site Coulombic interactions characterizing copper (Cu) atoms, effective Hubbard coefficients (*U-J*) were set to 6 eV for each. The Brillouin zone integration relied on a gamma-centered K-point mesh throughout the entire set of calculations. Stringent convergence thresholds were established, specifically 10^{-5} eV for electronic states and 0.02 eV·$Å^{-1}$ for ionic relaxations. To elucidate the phase stability of the Cu_2SnS_{3-x} compound, ab initio molecular dynamics (AIMD) simulation was performed. The simulations embraced the canonical ensemble (NVT) regulated by the Nosé–Hoover thermostat at a temperature of 300 K. The integration timestep was fixed at 2 fs, encompassing a dynamical trajectory spanning 10 ps. Considering the influence of solvent environments, the electrochemical carbon dioxide reduction reaction (CO_2RR) intermediates were evaluated via the Poisson-Boltzmann implicit solvent model, assuming a dielectric constant (ε) for water at 80. Orbital compositions resultant from the stable wavefunction were analyzed employing VASPKIT software[3], while LOBSTER package permitted intricate insights into the chemical bonding characteristics[4].

2. Supplementary Figures and Tables

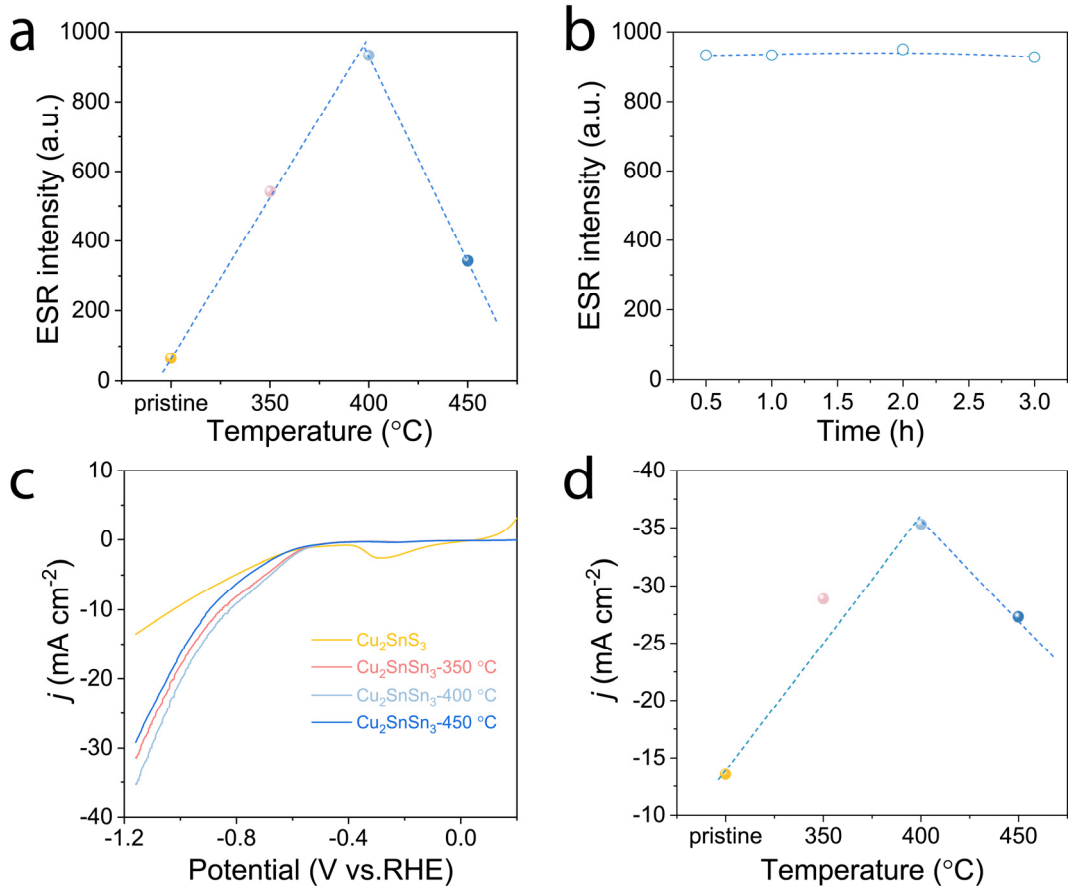

Fig.S1. The relationship between ESR intensity of sulfur vacancy and (a) annealing temperatures and (b) annealing times. (c) Cathodic currents of Cu_2SnS_3-*T* measured in 1M KOH with a scan rate of 10 mV s^{-1}. (d) The cathodic current densities of Cu_2SnS_3-T versus annealing temperatures.

I

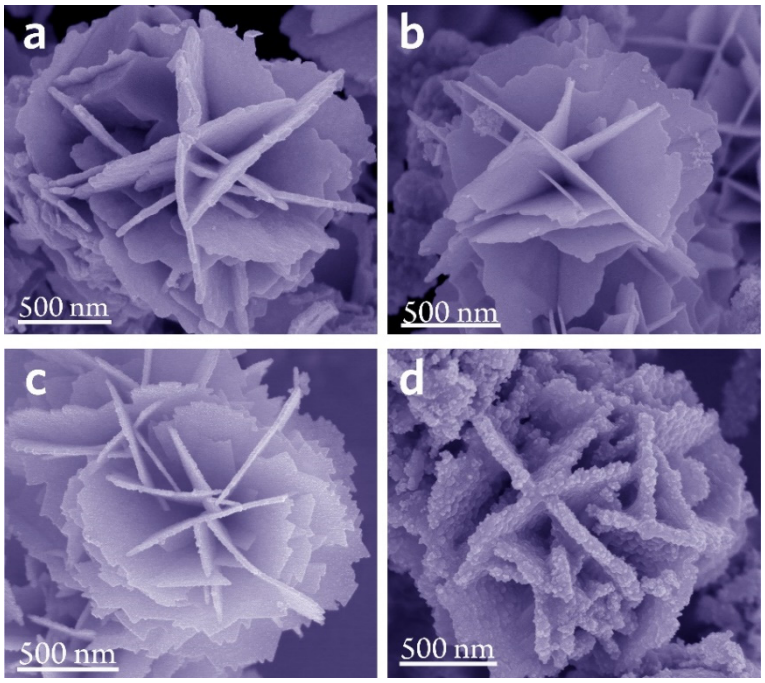

Fig.S2. SEM images of pristine Cu_2SnS_3 and Cu_2SnS_3-*T* (a) Cu_2SnS_3, (b) Cu_2SnS_3 -350 °C, (c) Cu_2SnS_{3-x},(d) Cu_2SnS_3- 450 °C.

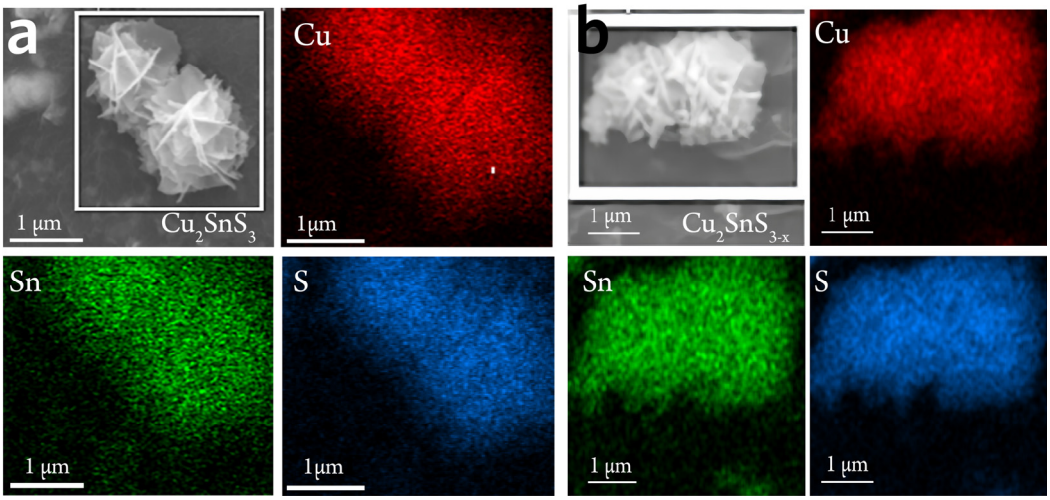

Fig.S3. The EDS spectra of (a) Cu_2SnS_3 and (b) Cu_2SnS_{3-x}.

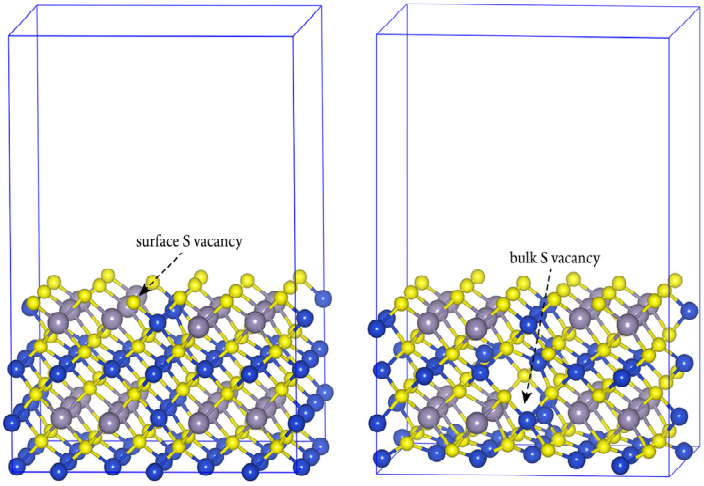

Fig.S4. (a) Models for surface and bulk surface vacancy calculation.

Note: $\Delta H_{\mathrm{f}} = E_{\mathrm{def}} + \mu_S - E_p$

Where E_{def} and E_{p} are the total energies of the Cu_2SnS_{3-x} and Cu_2SnS_3, μ_S is the atomic chemical potential of the S atom.

The formation energy of surface sulfur vacancy:

ΔH_f= -576.239eV-3.783+580.252eV=0.23eV

The formation energy of bulk sulfur vacancy:

ΔH_f= -574.117eV-3.783+580.252eV=2.352eV

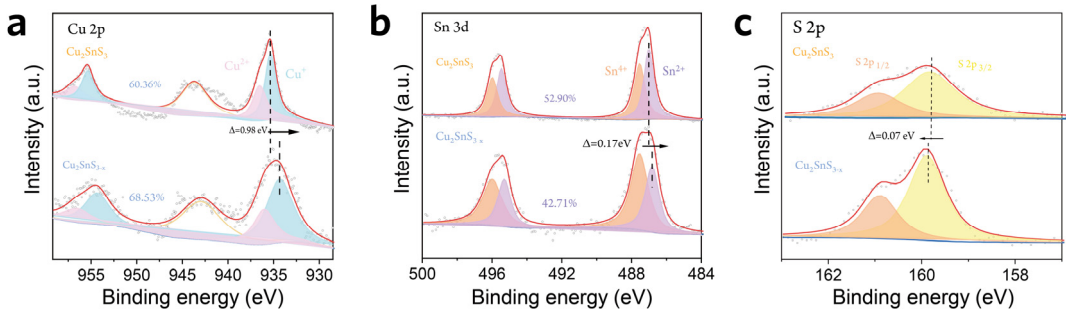

Fig.S5. Core-level XPS spectra of Cu 2*p*, Sn 3*d* and S 2p in Cu_2SnS_3 and Cu_2SnS_{3-x}.

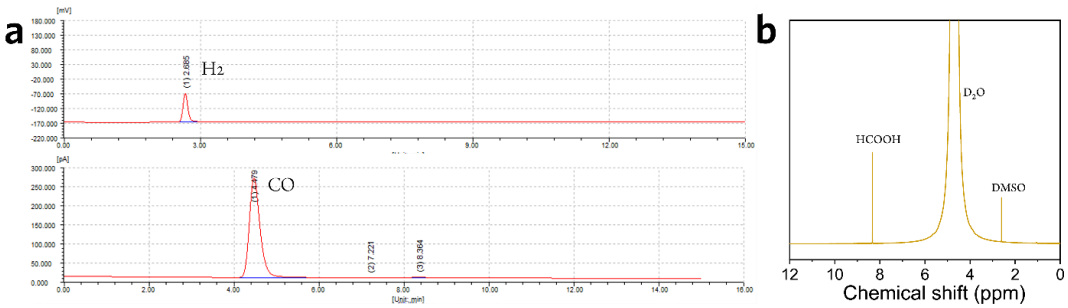

Fig.S6. Electrochemical CO_2 reduction products detected by (a) gas chromatography and (b) ^1H NMR spectra.

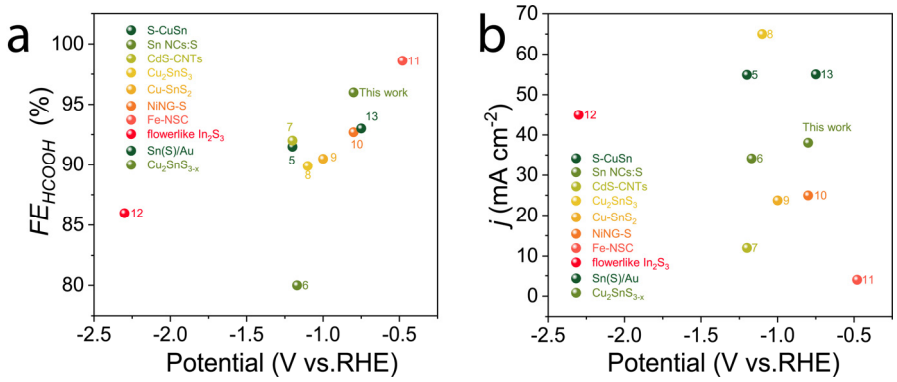

Fig.S7. Comparison of (a) *FE* and (b) j_{HCOOH} of Cu_2SnS_{3-x} with the other benchmarking HCOOH electrocatalysts in H-cell[5-13].

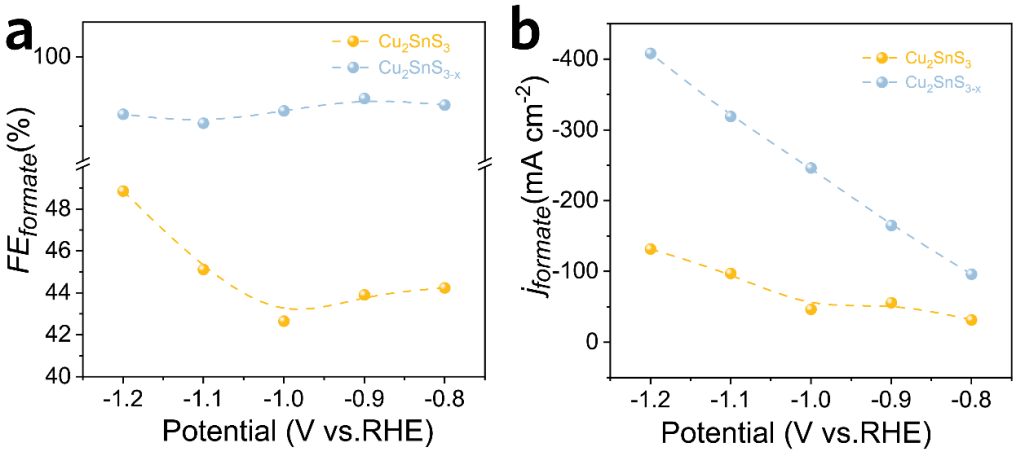

Fig.S8. The FE and $j_{formate}$ of Cu_2SnS_3 and Cu_2SnS_{3-x} in the flow cell.

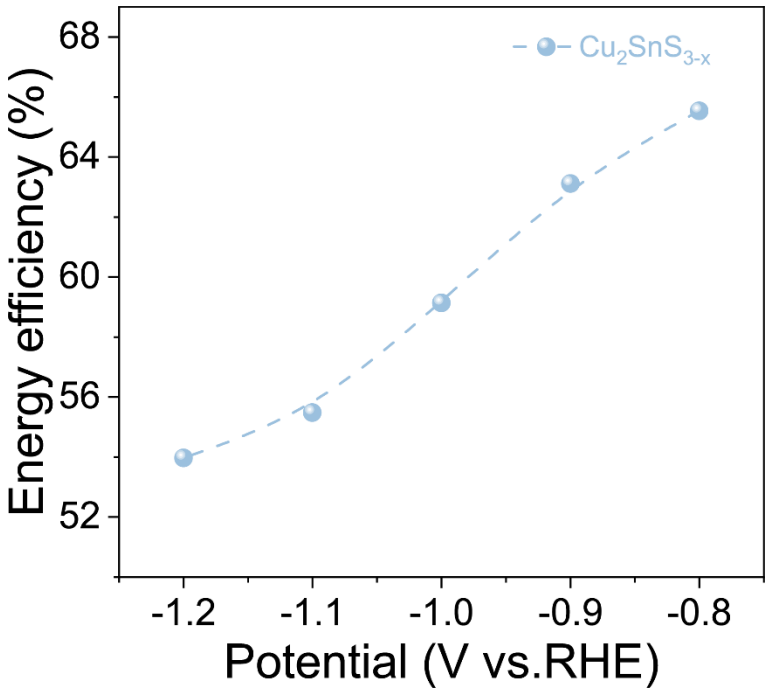

Fig.S9. The half-cell cathodic energy efficiencies (*EE*) of Cu_2SnS_{3-x} for CO_2-to-formate under various applied biases.

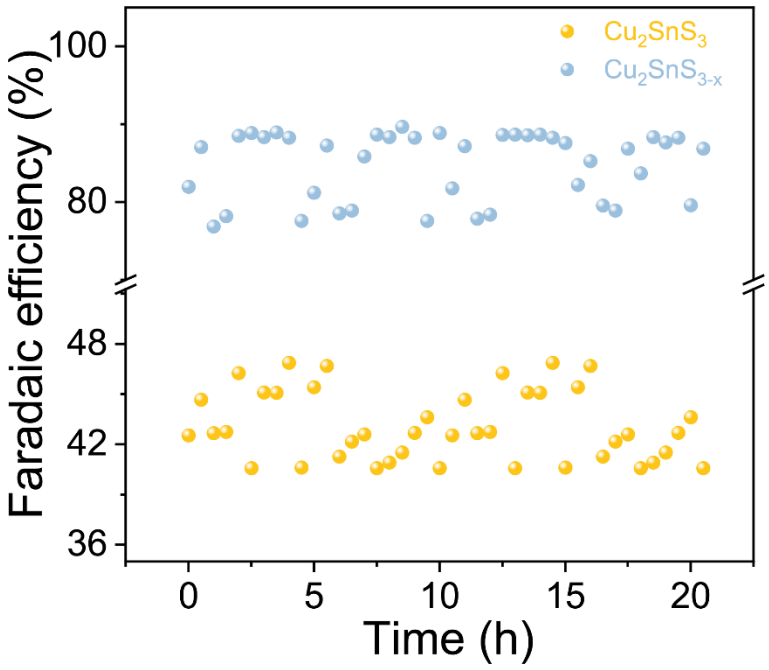

Fig.S10. The Faradaic efficiency of the formate as a function of time at -1.2 V vs. RHE.

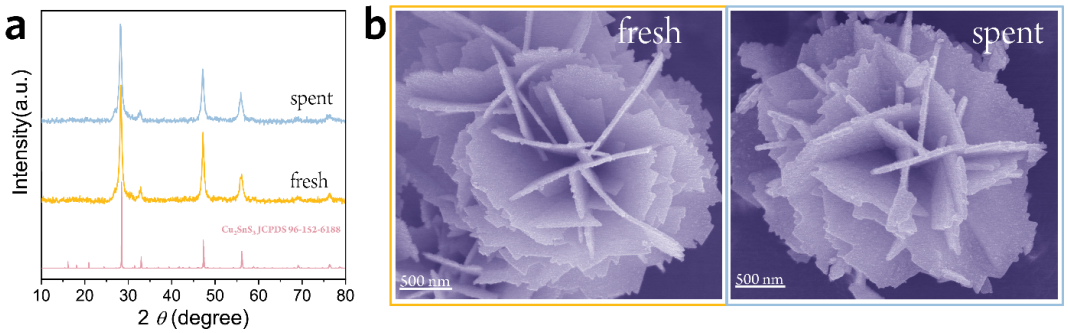

Fig.S11. (a) The XRD patterns and (b) SEM images of Cu_2SnS_{3-x} after 50 h electrochemical CO_2RR test compared to the pristine sample.

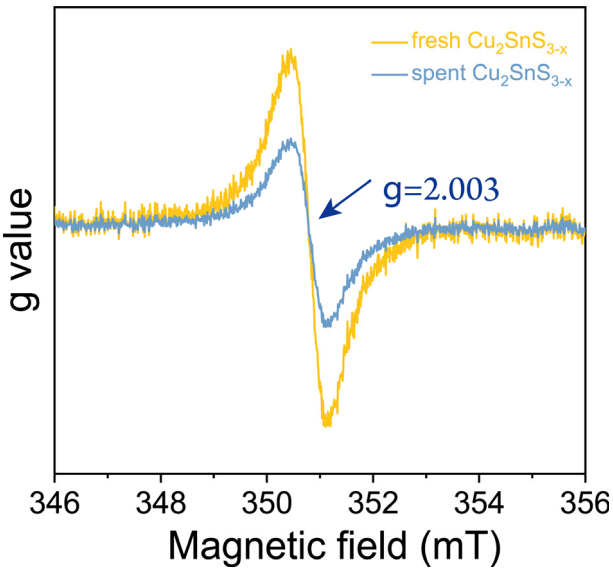

Fig.S12. The ESR spectra of pristine and spent Cu_2SnS_{3-x}.

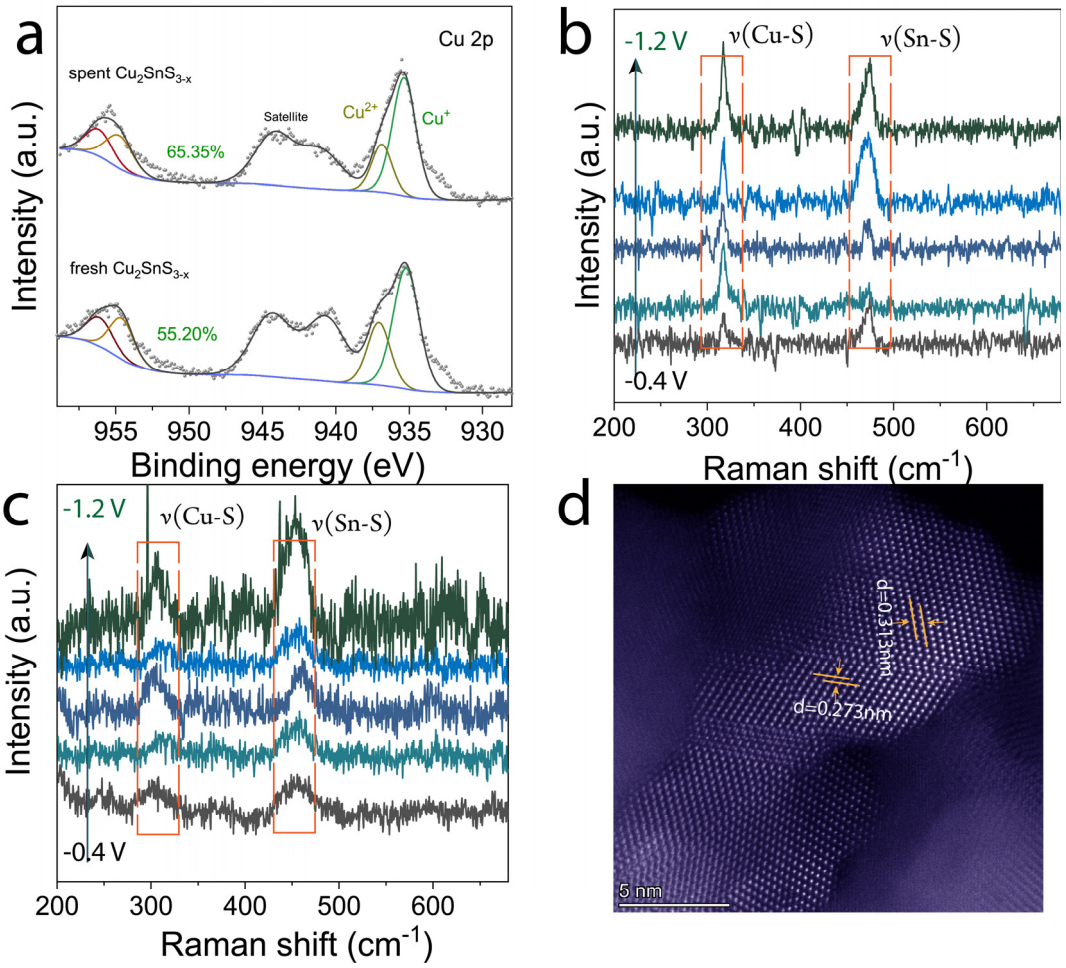

Fig.S13. (a) XPS spectra of Cu 2p of Cu_2SnS_{3-x} and Cu_2SnS_{3-x} after CO_2RR. (b) The in-situ Raman spectra of Cu_2SnS_3. (c） The in-situ Raman spectra of Cu_2SnS_{3-x}.(c)The HAADF-STEM image of Cu_2SnS_{3-x} after CO_2RR.

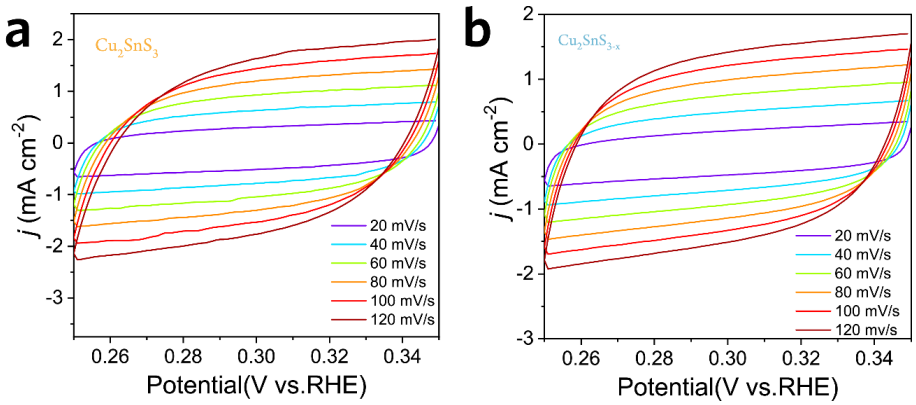

Fig.S14. Cyclic voltammetry at different scanning speeds for (a) Cu_2SnS_3 and (b) Cu_2SnS_{3-x}.

Note: CV curves were recorded in the non-Faraday region at six scan rates and for at least three cycles, the forward and reverse scans of the third cycle were selected to record the currents at a given potential, and the difference of these currents was plotted as a straight line relative to the scan rate. Half of the slope of this straight line is indicated as the double-layer capacitance.

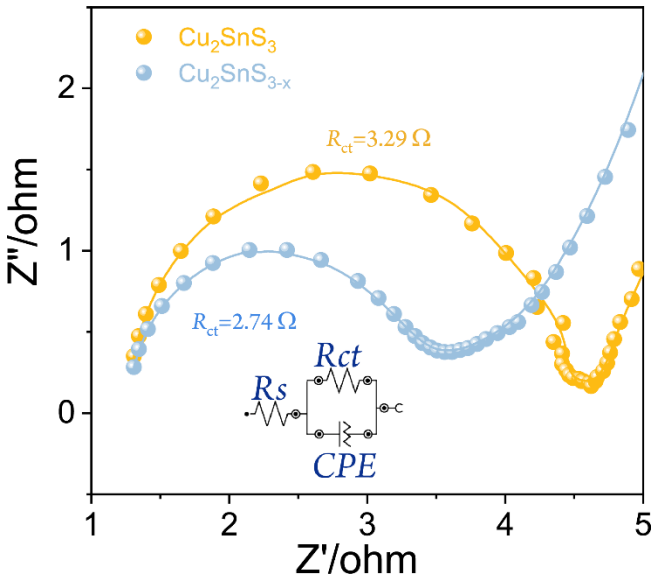

Fig.S15. The EIS spectra. Inset corresponds to its equivalent circuit, where R_{ct} represents the charge transfer resistance of catalysts and the date of fitting in Table S3.

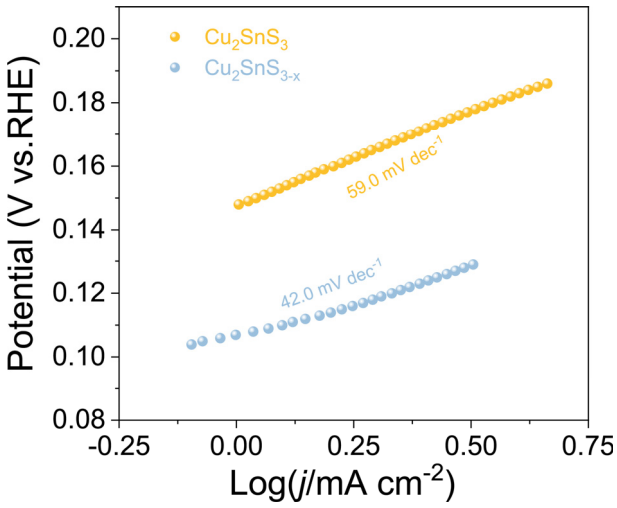

Fig.S16. The Tafel slops of catalyst.

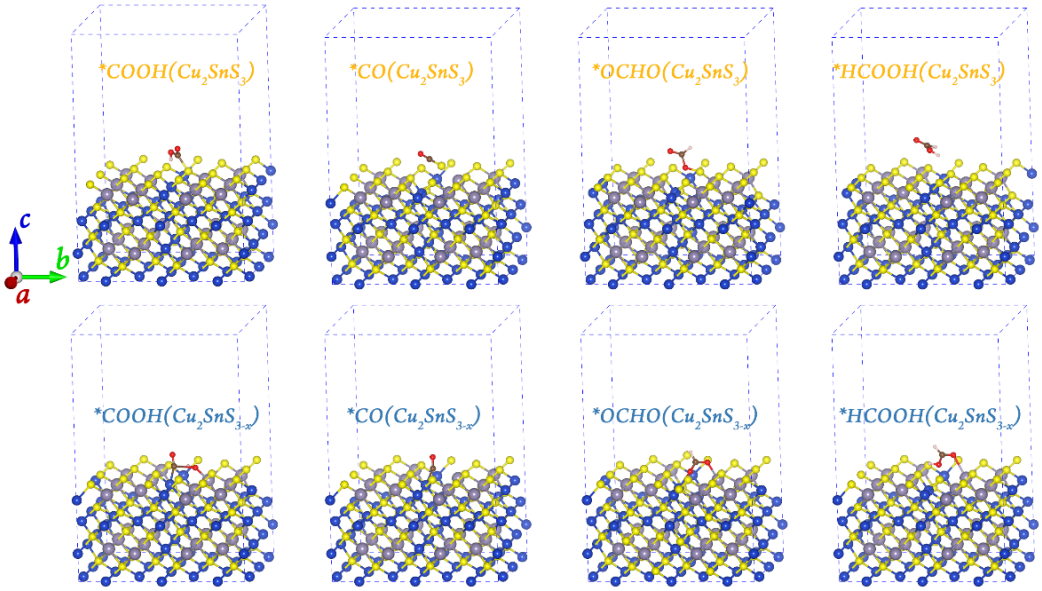

Fig.S17. The optimized geometries for the crucial intermediate in the electrochemical CO_2RR processes.

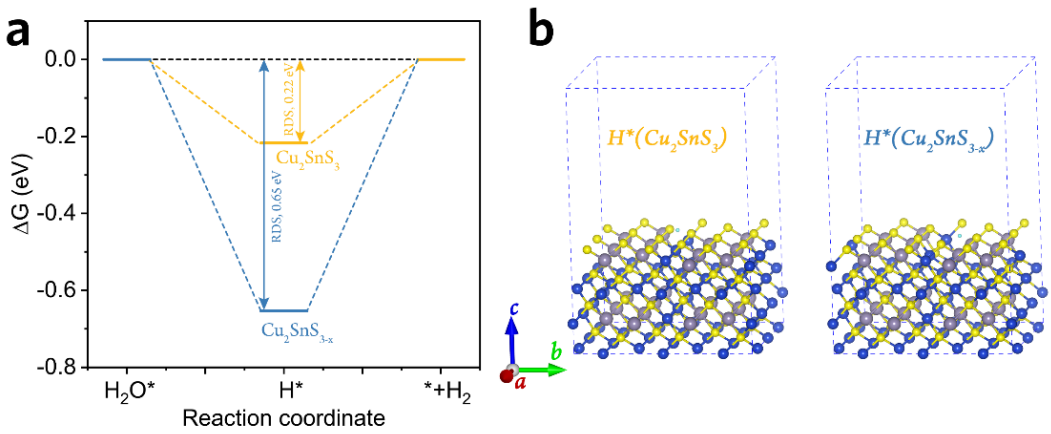

Fig.S18. (a) Gibbs free energy diagram for intermediates' evolution in HER, and (b) the corresponding optimized geometries. The data for the formation energy calculations are supplemented in Table S5.

Table S1. Elemental analysis for Cu_2SnS_3 and Cu_2SnS_{3-x} by ICP-MS.

Samples	Cu(wt%)	Sn (wt%)	S (wt%)	Atomic ratio of Cu: Sn:S
Cu_2SnS_3	37.15	34.72	28.13	2.008:1:3.013
Cu_2SnS_{3-x}	37.22	34.64	28.12	2.007:1:3.005

Table S2. The comparable generation rate and *EE* value of HCOOH relative to the other benchmarking catalysts for HCOOH production[14-20].

catalyst	Generation rate maximum	Energy efficiency maximum	Ref.
Sn/Cu foam	890.4 μmol $h^{-1}cm^{-2}$		14
3D tin electrode	113.3 μmol $h^{-1}cm^{-2}$	50%	15
Bi@Sn NPs	708.9 μmol h^{-1} cm^{-2}	59%	16
B-ArH_2-2	475 μmol h^{-1} cm^{-2}	71%	17
SnO_2 QWs		52.7%	18
In/N-dG	9.051 mmol h^{-1} cm^{-2}		19
Cu_2O/TiO_2	5237.8 μmol h^{-1} g^{-1}		20
Cu_2SnS_{3-x}	84.6 μmol h^{-1} cm^{-2} 16926 μmol h^{-1} g^{-1}	65.5%	This work

Table S3. Date of EIS fitting.

catalyst	*Rs*	*CPE-T*	*CPE-P*	*Rct*
Cu_2SnS_3	1.207	7.71E-06	0.94829	3.285
Cu_2SnS_{3-x}	0.90806	4.04E-05	0.79466	2.743

Table S4. Ground state energy calculated by DFT, *ZPE*, and *TS* correction for optimized crucial intermediates evolution on Cu_2SnS_3 and Cu_2SnS_{3-x}.

Species	E_{DFT} (eV)	*ZPE* (eV)	*TΔS* (eV)	ΔG/eV
*(Cu_2SnS_3)	-580.252			
*OCHO(Cu_2SnS_3)	-605.862	0.66	0.13	-605.332
*COOH(Cu_2SnS_3)	-606.042	0.67	0.14	-605.512
*HCOOH(Cu_2SnS_3)	-609.912	1.05	0.30	-609.162
*CO(Cu_2SnS_3)	-595.522	0.24	0.10	-595.382
*(Cu_2SnS_{3-x})	-576.239			
*OCHO(Cu_2SnS_{3-x})	-603.359	0.70	0.15	-602.809
*COOH(Cu_2SnS_{3-x})	-606.189	0.69	0.18	-605.679
*HCOOH(Cu_2SnS_{3-x})	-606.719	1.03	0.22	-605.909
*CO(Cu_2SnS_{3-x})	-591.749	0.27	0.15	-591.629
CO_2	-22.95	0.31	0.66	-23.30
CO	-14.78	0.13	0.60	-15.25
H_2	-6.76	0.27	0.40	-6.89
H_2O(l)	-14.22	0.56	0.67	-14.33

Table S5. Total energies of clean Cu_2SnS_3 and Cu_2SnS_{3-x}., as well as energies of the most stable absorption geometries for H* intermediate.

Surfaces	*E*(*)/eV	*E*(H*)/eV	*ZPE* (eV)	*TΔS* (eV)
Cu_2SnS_3	-580.252	-584.172	0.28	0.03
Cu_2SnS_{3-x}	-576.239	-580.529	0.21	0.02

References

1 J.-C. Liu, F. Luo, J. Li, J. Am. Chem. Soc.,2023, **46**, 25264-25273.
2 C. E. Ekuma, V. I. Anisimov, J. Moreno, M. Jarrell, Eur. Phys. J. B,2014, **87**, 23.
3 V. Wang, N. Xu, J.-C. Liu, G. Tang, W.-T. Geng, Comput. Phys. Commun.,2021, **267**, 108033.
4 S. Maintz, V. L. Deringer, A. L. Tchougréeff, R. Dronskowski, J. Comput. Chem., 2016, **37**, 1030-1035.
5 K. Li, J. Xu, T. Zheng, Y. Yuan, S. Liu, C. Shen, T. Jiang, J. Sun, Z. Liu, Y. Xu, M. Chuai, C. Xia, W. Chen, ACS Catal., 2022, **12**, 9922-9932.
6 X. Wang, F. Li, W.-J. Yin, Y. Si, M. Miao, X. Wang, Y. Fu, Appl.catal.B, 2022, **304**, 120936.
7 Wang, Z. Wang, R. Yang, J. Duan, Y. Liu, A. Nie, H. Li, B. Y. Xia, T. Zhai, Angew. Chem. Int. Ed*.,* 2021*,* **60**, 22940-22947.
8 Chen, S. Wan, L. Zhong, D. Liu, H. Yang, C. Li, Z. Huang, C. Liu, J. Chen, H. Pan, D. S. Li, S. Li, Q. Yan, B. Liu, Angew. Chem. Int. Ed., 2021, **60**, 26233-26237.
9 B. Wei, Y. Xiong, Z. Zhang, J. Hao, L. Li, W. Shi, Appl. Cata. B, 2021, **283**, 119646.
10 Chen, X. Li, C. W. Kao, T. Luo, K. Chen, J. Fu, C. Ma, H. Li, M. Li, T. S. Chan, M. Liu, Angew. Chem. Int. Ed*.,* 2022*,* **61**, e202206233.
11 Feng, H. Gao, J. Feng, L. Liu, S. Zeng, H. Dong, Y. Bai, L. Liu, X. Zhang, ChemCatChem, 2019, **12**, 926-931.
12 Zheng, P. De Luna, F. P. García de Arquer, B. Zhang, N. Becknell, M. B. Ross, Y. Li, M. N. Banis, Y. Li, M. Liu, O. Voznyy, C. T. Dinh, T. Zhuang, P. Stadler, Y. Cui, X. Du, P. Yang, E. H. Sargent, Joule, 2017, **1**, 794-805.
13 H, Tao, T. Jia, L. Zhang, X. Li, P. Li, Y. Zhou, C.Zhai, J. Colloid Interf. Sci., 2024, **655**, 909–919.
14 Y. Yan, Y. Peng, Y. Song, R. Wang, H. Wang, Z. Bian, Chemosphere, 2022, **301**, 134704.
15 Qin, H. Wang, F. Peng, H. Yu, Y. Cao, J. CO_2 Util*.,* 2017*,* **21**, 219-223.
16 Xing, X. Kong, X. Guo, Y. Liu, Q. Li, Y. Zhang, Y. Sheng, X. Yang, Z. Geng, J. Zeng, Adv. Sci., 2020, **7**, 1902989.
17 R.C. Cui, Y. X. Duan, J. Y. Xie, Q. Jiang, Adv. Sustain. Syst*.,* 2023, 2300348.
18 S. Liu, J. Xiao, X. F. Lu, J. Wang, X. Wang, X. W. D. Lou, Angew. Chem. Int. Ed., 2019, **58**, 8499-8503.
19 J. Bi, P. Li, J. Liu, Y. Wang, X. Song, X. Kang, X. Sun, Q. Zhu, B. Han, Angew. Chem. Int. Ed*.,* 2023, **62**, e202307612.
20 Q. Zhu, Z. Deng, H. Xie, M. Xing, J. Zhang, ACS Catal., 2023, **13**, 3254-3262.